metals

MDPI

Article

Characterization of the Microstructure Evolution of Ni-Based Superalloy at Liquidus Temperature by Electromagnetic Field

Zhongtang Gao [1,*], Jinqiang Tan [2], Wei Guo [1], Chuanwei Zhang [1] and Wu Zhang [1]

[1] School of Mechanical Engineering, Xi'an University of Science and Technology, Xi'an 710054, China; weiguo123@xust.edu.cn (W.G); zhanggchuanwei@xust.edu.cn (C.Z); zhangwugang2008@xust.edu.cn (W.Z)

[2] State Key Laboratory of Solidification Processing, Northwestern Polytechnical University, Xi'an 710054, China; jayson2005@126.com

* Correspondence: zhongtanggao@xust.edu.cn; Tel.: +86-29-85583157

Received: 19 August 2018; Accepted: 21 September 2018; Published: 23 September 2018

Abstract: The effect of isothermal treatment temperatures and isothermal treatment time on the microstructure was studied. The results showed that the globular and equiaxed grains with the average grain size of 60 μm and the shape factor of circle of 0.95 can be obtained when the melt of Ni-Cr-W superalloy was subjected to the heat treatment of 10 min at 1400 °C. The quenching results showed the volume fraction of the eutectic phase was the largest and the volume fraction of primary γ phase was the smallest after the isothermal treatment of 1400 °C. The optimal melt treatment temperature and time were 1400 °C and 10 min, respectively. Moreover, the effect of electromagnetic field on the solidification was also investigated. It was demonstrated that applying electromagnetic field was beneficial to the uniform temperature, solute field and the high density of the secondary nuclei, which contributed to grain refinement.

Keywords: melt treatment; solidification; electromagnetic field; Ni-Cr-W superalloy; microstructure

1. Introduction

In the casting of Ni-based superalloys, it is a common industrial practice to promote the formation of a fine, uniform and equiaxed grain microstructure [1]. This step is critical since a refined microstructure could reduce hot tearing, improve feeding to eliminate shrinkage porosity, and finer distribution of second phase and microporosity [2,3].

Some approaches could achieve grain refinement, including electromagnetic stirring [4], low-temperature casting [5], melt-superheating treatment [6], semi solid casting [7], inoculation and dynamic nucleation [8,9]. The most common method used for obtaining fine and uniform grain microstructures is controlling the melt treatment temperature and time [10]. The other method is dynamic nucleation, which can be achieved by the application of localized forced convection coupled with cooling to create secondary nuclei [11]. Generally, equiaxed and spherical grains can be obtained by the application of an electromagnetic field. When the effective nucleation substrates could be ignored, dendrite fragments are thought to be the major reason for the equiaxed grain formation [12]. Therefore, the fragmentation caused by the forced convection is also an important factor for the grain refinement [13,14]. However, some researchers think that the forced convection cannot break the dendrite arm under normal solidification conditions [15,16]. Hence, the main source of nucleation site and growth mechanism of nuclei still require further investigation. Moreover, the mechanism of the grain refinement by electromagnetic field has not been methodically studied.

It is well known that the melt parameters have a considerable influence on solidification structure. However, the relationship between the melt parameters and the microstructure has not been thoroughly

studied. A series of problems still need to be clarified. For example, what kind of isothermal treatment temperature and isothermal treatment time can achieve the optimized microstructure? To disclose the effect of melt parameters including isothermal treatment temperatures and isothermal treatment times on solidification microstructures, the present work applied the rapid quenching method to investigate the combined effects of various isothermal treatment temperature and time on the solid fraction, particle density and particle size of the secondary nuclei. In addition, the effect of electromagnetic field on the microstructure has been studied.

2. Material and Methods

The nominal composition (wt.%) of the alloy used in this study is Ni-20Cr-18W-1Mo [17]. The measured solidus and liquidus temperatures of the alloy are 1355 °C and 1400 °C, respectively. Ni-Cr-W superalloy is a kind of solid solution strengthening alloy that the atoms solved into nickel substrate and the material has not responded with Al_2O_3 crucible.

The different microstructures are obtained by various isothermal treatment temperatures as follows. The sample was placed in an alumina crucible sized (30 mm in diameter and 50 mm in length) and then heated by induction coil. The application of electromagnetic field was controlled by the medium frequency induction heating power source. The parameters of the heating power are field strength (H = 0.2 T), frequency (f = 5 kHz) and power (P = 20 kW). Experiment without electromagnetic field is as follows. Because the graphite has good thermal conductivity, electrical conductivity and non-magnetic properties. The graphite sleeve is used to shield the electromagnetic field by the method that the graphite sleeve is wrapped around the ceramic crucible. The melt in the ceramic crucible covered with graphite is heated by the thermal radiation. After the chamber was cleaned to a vacuum of 2×10^{-6} Pa, it was filled with high purity argon (99.999%) to 1.1×10^5 Pa. Approximately 30 g of superalloy (the melt covered with some pieces of B_2O_3 glass) was melted in a ceramic crucible (30 mm in diameter and 50 mm in length) at 1500 °C in an induction coil. The alloy was then removed from the furnace and allowed to slowly cool down to the experimental temperatures (1480 °C, 1420 °C, 1410 °C, 1400 °C and 1390 °C) and kept at different temperatures for 10 min before air cooling cast. B_2O_3 glass was used to prevent oxidation placed in the top of the melt. The quenching medium used in this study is water.

Microstructures of the samples cast with different conditions were characterized. Standard metallography procedures were cut, prepared by mechanical polishing, followed by electro-polishing using solution of 20% H_2SO_4 + 80% methanol (vol.%). The grain distribution and microstructure were observed using scanning electron microscope (SEM) at selected locations. The microstructure morphology was analyzed by Jeol JSM-7000F SEM (ZEISS, Oberkochen, Germany). Samples for SEM quenching from the different isothermal temperatures (1480 °C, 1420 °C, 1410 °C, 1400 °C and 1390 °C) were performed simply from the crucible into saline water.

3. Results and Discussion

3.1. Effects of Isothermal Treatment Temperature on the Microstructures

Figure 1 shows the microstructure with different isothermal treatment temperatures. The results in Figure 1 demonstrate that the isothermal treatment temperature has an impact on the microstructure. There are three different kinds of solidification microstructures, as shown in Figure 1. Typical microstructures of Figure 1a–c samples are the dendritic and coarsened grains, and dendrites have a certain orientation and grow along the direction of heat flow, whereas a typical microstructure of Figure 1d sample is the equiaxed, globular and non-dendritic grains. The typical microstructure of Figure 1e sample is the rose shape grain. When the melt is dealt with isothermal treatment in 1480 °C, some dendrites are rather coarse with a well-developed second dendrite arm. With the decrease of isothermal treatment temperature from 1480 °C to 1420 °C and 1410 °C, the well-developed second dendrite arm disappears. Meanwhile, there are some globular grains distributed in the

dendritic grains. When the melt is dealt with isothermal treatment in 1400 °C, there are only the globular, equiaxed grains distributed in the solidification structure, and the average grain size is 60 μm. With the decrease of isothermal treatment temperature from 1400 °C to 1390 °C, several rose-shaped grains can be observed in Figure 1e.

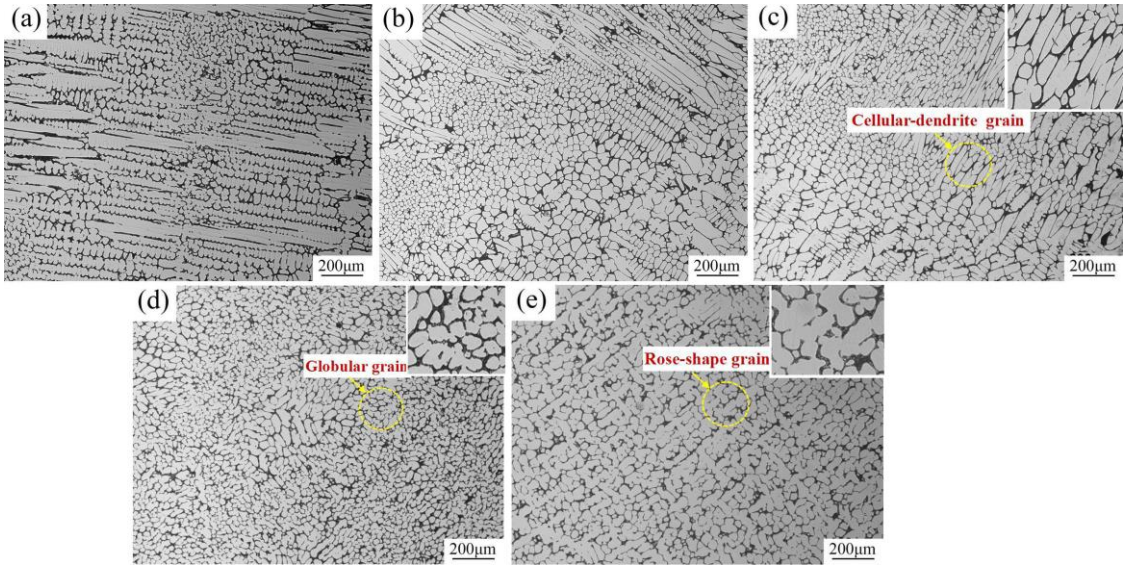

Figure 1. Effect of various isothermal treatment temperatures on the microstructure of Ni-Cr-W superalloy: (**a**) 1480 °C; (**b**) 1420 °C; (**c**) 1410 °C; (**d**) 1400 °C; (**e**) 1390 °C.

In order to get more accurate size and shape of the grain obtained at different temperatures, the grain size was measured by the Jeffries method for estimating the average grain size according to the National Standard of the PR China, GB/T6394-2004. Grain size numbers at various isothermal temperatures are also presented schematically, i.e., as shown in Figure 2a. The shape factor of circle (CSF) is employed to determine the roundness of grain. The value of CSF is between 0 and 1. The shape of grain is close to sphere as the value of CSF is close to 1. The results of CSF at various isothermal temperatures are shown in Figure 2b.

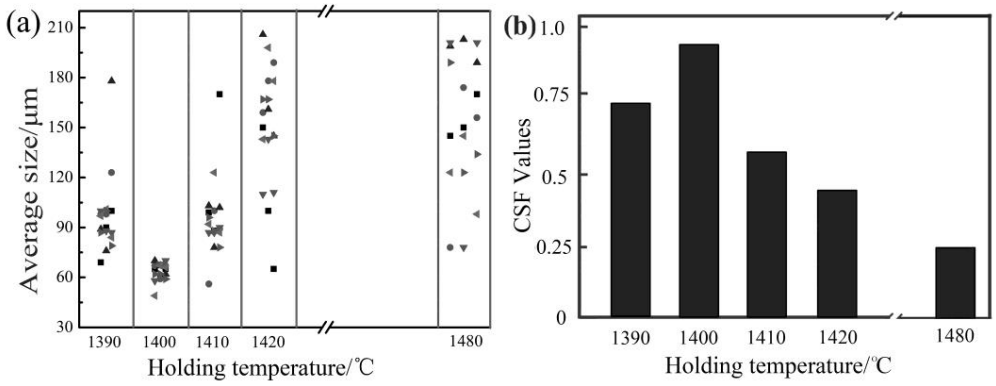

Figure 2. Analysis of solidification microstructure by various isothermal treatment temperatures of Ni-Cr-W superalloy: (**a**) the average particle size; (**b**) the shape factor of circle.

It is confirmed that the grains holding at 1400 °C are smallest with an average size of 68 μm, and the value of CSF is 0.95. The maximum and minimum size of grain holding at 1480 °C are 200 μm and 70 μm, respectively, and the value of CSF is 0.25. The maximum and minimum size of grain holding at 1420 °C are 170 μm and 60 μm, respectively, and the value of CSF is 0.40. The average size of grain holding at 1410 °C and 1390 °C is 90 μm, and the values of CSF are 0.55 and 0.72, respectively.

The result demonstrates that the sizes and shapes of the grain at the liquidus temperature (1400 °C) are homogeneous. In contrast, the sizes and shapes of the grain above and below the liquidus temperature are not homogeneous. It is universally considered that when the melt is dealt above and below the liquidus temperature, there is no cluster in the melt that serves as nucleation, at the same time, the temperature field becomes more unevenly [18]. These factors easily lead to formation of coarse dendrites. When the melt is dealt near the liquidus temperature, the melt temperature field becomes more evenly, which also makes phase fluctuation become small [19,20]. Meanwhile, the quantities of clusters increase in the melt and the distribution of clusters is more evenly. Uniform temperature and solute field allow more particles of a suitable size to be active in heterogeneous nucleation and restrict the growth of crystal [21]. This in turn benefits to the formation of equiaxed and non-dendritic grains.

To understand the grain refinement behavior under the influences of different isothermal treatment temperatures and the effects of the particle density of the secondary nuclei on the final cast microstructure, a rapid quenching method is used to investigate the effect of isothermal treatment temperature on the solid fraction, particle density and particle size of the secondary nuclei. The representative microstructures of quenched samples with different processing conditions are given in Figure 3. The melt of 1480 °C and 1420 °C is still liquid state before quenching in this temperature range, and the quenching microstructure is composed of very small dendrite microstructure, as shown in Figure 3a,b. The quenching microstructure at 1420 °C is composed of incomplete dendritic microstructure and developed isometric dendrite microstructure inherited from formed nuclei but not grown in time. The residual liquid and primary solid phase are observed in the solidified tissue quenching microstructure, as shown in Figure 3c. The primary phase dispersed in the quenching microstructure is small in size in Figure 3d. Meanwhile, the volume fraction of the residual liquid phase is the same as that of the primary solid phase. These results demonstrate that there are a large number of atoms cluster in the 1400 °C isothermal melt served as the crystal nucleus in subsequent solidification, so that the primary solid phase can be dispersed in the quenching microstructure by increasing the nucleation rate. The quenching microstructure at 1390 °C is composed of a large number of primary solid phase and a small amount of residual liquid as shown in Figure 3e. This is because there is a certain amount of solid phase in the melt before quenching and the residual liquid phase quickly changes to solid phase in the subsequent solidification.

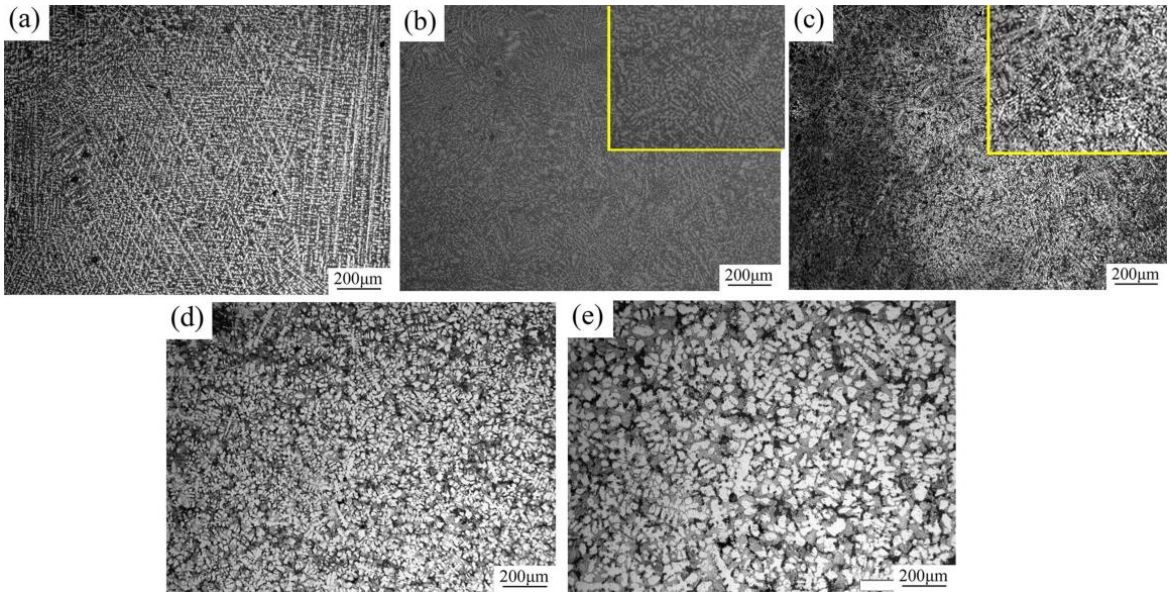

Figure 3. Effect of various isothermal treatment temperatures on the quenching microstructure of Ni-Cr-W superalloy: (**a**) 1480 °C; (**b**) 1420 °C; (**c**) 1410 °C; (**d**) 1400 °C; (**e**) 1390 °C.

To study the effect of isothermal treatment temperatures on the morphology of carbide precipitation in the quenching microstructure, the phase morphologies of the three isothermal treatment temperatures near the liquid are shown in Figure 4. The eutectic precipitated phase in a fishbone shape is obtained in the isothermal treatment temperature of 1410 °C, as shown in Figure 4a. These eutectic precipitated phases would crystallize with matrix in the subsequent solidification. The lamella of eutectic precipitated phase in 1400 °C is smaller than that of 1410 °C, as shown in Figure 4b. The quenching microstructure in 1390 °C is composed of the cord-shaped and fish-bone precipitated phase in Figure 4c. This is due to the following reasons: (I) the solute W element is slanted in the grain boundary; (II) the Ni element is slanted in the grain; (III) the eutectic phase rich in Ni and W elements is precipitated during rapid quenching.

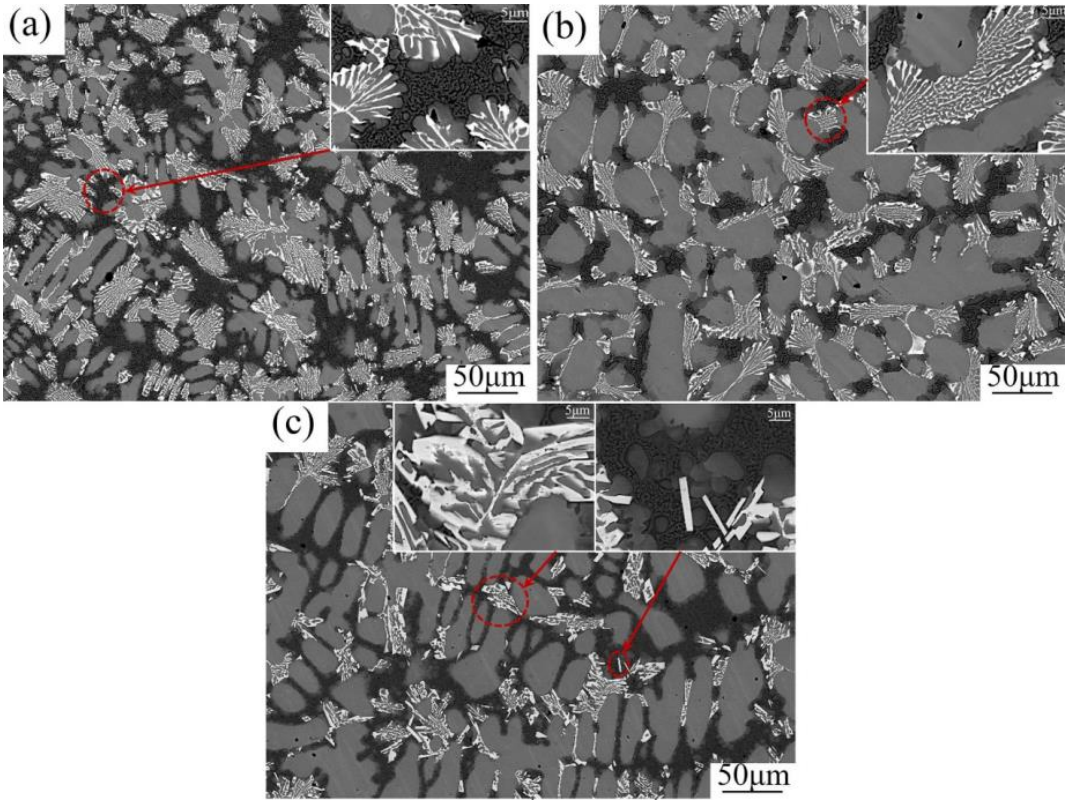

Figure 4. The phase morphology after various isothermal treatment temperatures of Ni-Cr-W superalloy: (**a**) 1410 °C; (**b**) 1400 °C; (**c**) 1390 °C.

To obtain quantitative variation laws about the volume fractions of eutectic phase and primary γ phase affected by isothermal treatment temperature, the quantitative analysis results of these solid particles are shown in Figure 5 for the solid fraction. The volume fraction is calculated by the method that the quenching microstructure are binarized, and the eutectic phase is distinguished from the primary γ phase [22].

The volume fractions of the eutectic phase of the different samples obtained from the temperature of 1420 °C, 1400 °C and 1390 °C are 9.77%, 12.3% and 11.39%, respectively. The volume fractions of primary γ phase of the different samples obtained from the temperatures of 1420 °C, 1400 °C and 1390 °C are 34.01%, 30.04% and 39.83%, respectively, as shown in Figure 5. The result shows that the volume fraction of the eutectic phase is the largest and the volume fraction of primary γ phase is the smallest after the isothermal treatment of 1400 °C. This is due to the important factor that the solute and temperature field of the liquidus isothermal treatment is more uniform [23,24], and the uniform distribution of solute elements make the eutectic phase rich in W and Ni elements increase and the primary γ phase decrease.

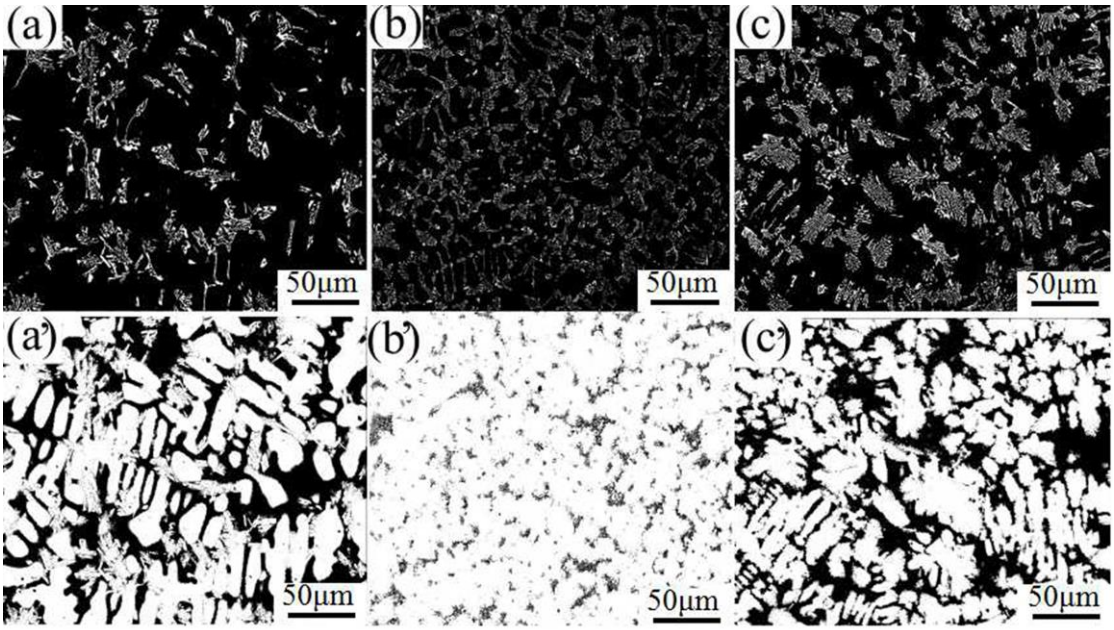

Figure 5. The SEM image after binarization processing isothermal treatment at various temperatures of Ni-Cr-W superalloy: (**a**) 1420 °C; (**b**) 1400 °C; (**c**) 1390 °C, (**a**–**c**) Eutectic; (**a′**–**c′**) γ phase.

3.2. Effects of Isothermal Treatment Time on the Microstructures

Figure 6 shows the microstructures of different isothermal treatment times at 1400 °C.

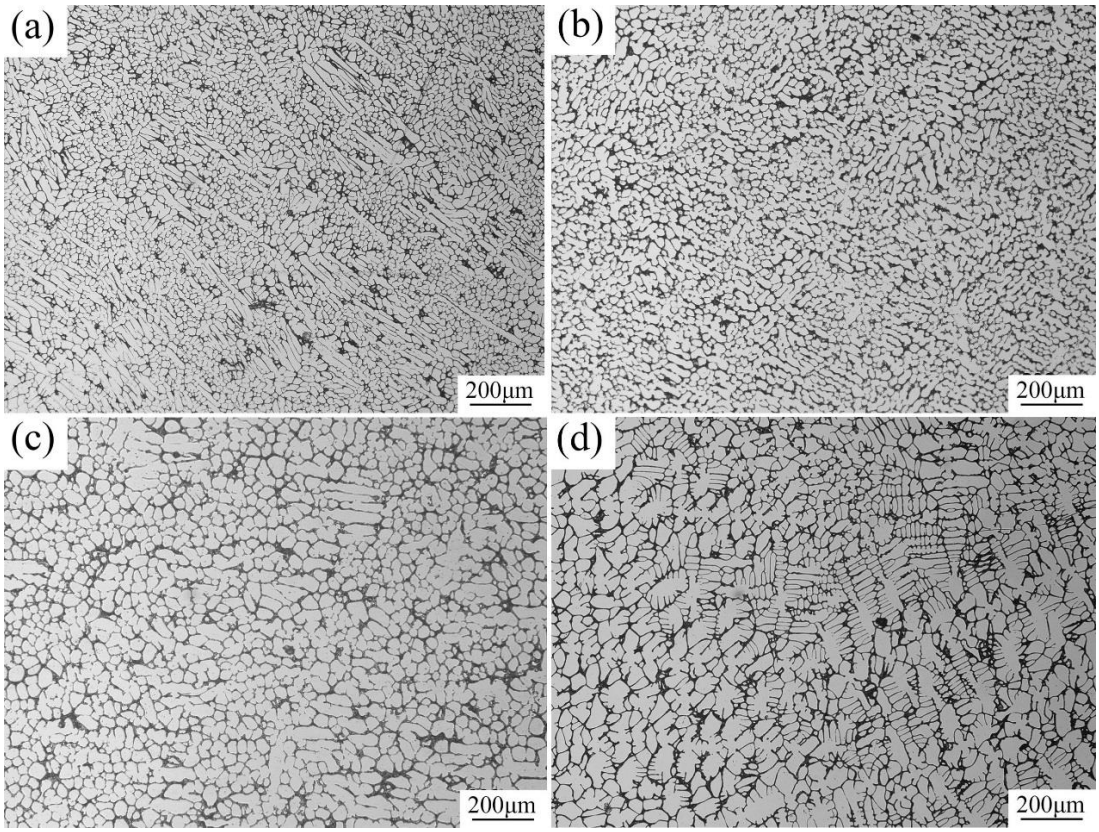

Figure 6. Effect of isothermal treatment time at 1400 °C on the microstructure of Ni-Cr-W superalloy: (**a**) 2 min; (**b**) 5 min; (**c**) 10 min; (**d**) 15 min.

Typical microstructure of Figure 6a is principally cell crystal and coarse equiaxed dendritic grain, and the grain size is small and uneven. Typical microstructure of Figure 6b is globular and non-dendritic grains instead of principally cell crystal and coarse equiaxed dendrites when the isothermal treatment time extends to 5 min, and the grain size is small and even. Typical microstructure of Figure 6c is globular and non-dendritic grains when the isothermal treatment time extends to 10 min, but the grain size is small and even, and the grain size of Figure 6c increases with the increase of isothermal treatment time but is slightly affected by isothermal treatment time. The value of CSF approaching 1 demonstrates that the globular grains have the best roundness and uniformity. Typical microstructure of Figure 6d is principally cell crystal and coarse equiaxed dendritic grain when the isothermal treatment time extends to 15 min, and the grain size is large and uneven.

Comparing the different processing conditions, it is observed that the typical microstructure changes from certain orientation of cell crystals to equiaxed or spheroidal crystal and finally to rosaceous grain as the isothermal treatment time increase from 5 min to 15 min. Meanwhile, the grain size changes from large to small and finally to large with the increase of isothermal treatment time. It shows that the microstructure is the optimal state in terms of size and uniformity when the isothermal treatment time is 10 min. The isothermal treatment time of 5 min makes the melt temperature and solute fields less uniform, leads to the subsequent solidification which has a certain orientation along the temperature gradient. Meanwhile there are fewer nucleation in the melt. The isothermal treatment time is too long, although solute field and temperature field is more uniform, but the potential nucleation is combined growth and maturation in the process of heat preservation, which makes the number of nucleation become smaller. The isothermal treatment time of 10 min not only improves the uniformity of solute and temperature field in the melt, it also reduces the solidification heat transfer caused by temperature fluctuations. Uniform temperature and solute field allow more particles of a suitable size to be active in heterogeneous nucleation and restrict the growth of crystal.

3.3. Effects of Electromagnetic Field on the Microstructures

The representative solidification microstructures with different processing conditions are shown in Figure 7. One can see that the Ni-Cr-W superalloy is a typical cast dendrite and inter-dendrite microstructure without electromagnetic field (EMF) processing. The solidification structures with EMF are more refined. Consequently, the stirring current and Peltier thermal effect caused by EMF are feasible and effective to refine grains for Ni-Cr-W superalloy. The solidification microstructure is composed of dendrites and columnar crystals when the melt is dealt with isothermal treatment at 1420 °C and 1390 °C. Some dendrites are rather coarse with well-developed primary trunks as shown in Figure 7a,c. With the application of EMF, the coarse dendrites become smaller as shown in Figure 7d,f. The solidification microstructure is composed of columnar and fine globular grains when the melt is dealt with isothermal treatment at 1400 °C. Without EMF, columnar dendrites along the cooling direction are yielded on the surface of the sample, and coarse equiaxed grains are produced in the center of the sample, as shown in Figure 7b, while complete fine equiaxed grains with the average grains size of about 60 μm are produced in the whole sample solidified with low voltage pulsed magnetic field, as shown in Figure 7e. By applying the EMF technique, the problems of conventional casting can be eliminated. As for uniform the microstructure in all the nuclei would be able to survive and grow. Meanwhile, the existence of EMF improves the uniformity of the solute and temperature fields [25,26]. These result in a fine and uniform microstructure. So, an ingot with fine and uniform microstructure is achieved.

In fact, EMF not only improves the uniformity of solute and temperature fields, but also makes the concentration gradient decrease at the front of the solid/liquid interface and improves the stability of the solid/liquid interface [27], which is beneficial to the grain refinement. Therefore, in order to reveal the stability of the solid/liquid interface under the effect of EMF, we introduce the effect of EMF on the stability of spherical grains.

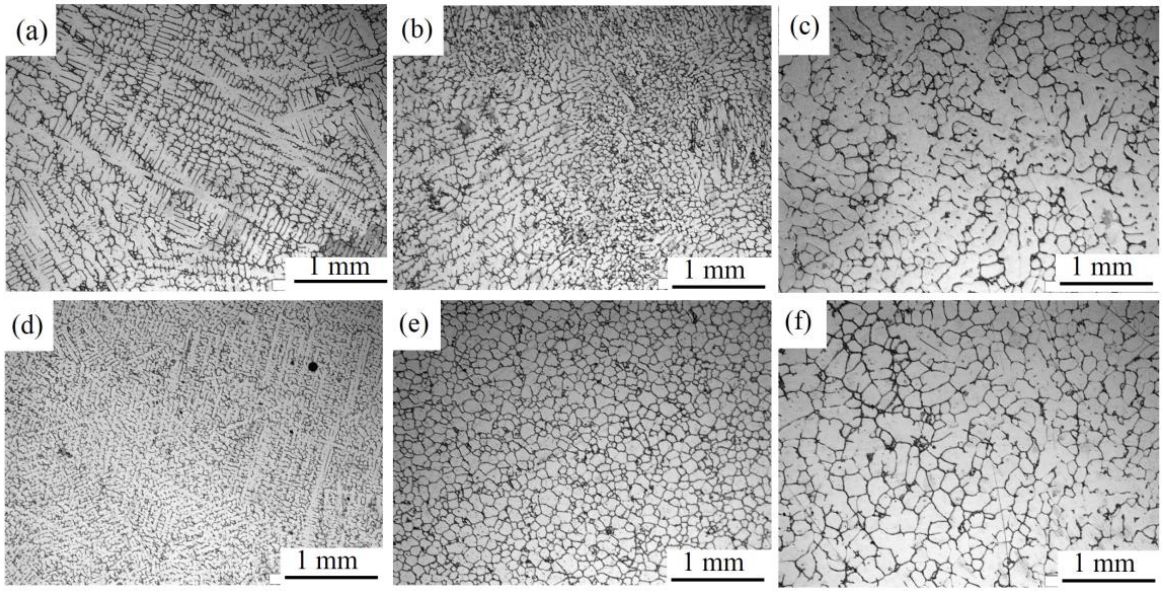

Figure 7. Microstructure of Ni-Cr-W superalloy by isothermal treatment at various temperatures with various conditions: (**a**–**c**) Non-sheared by electromagnetic field (EMF); (**d**–**f**) sheared by electromagnetic field; (**a**,**d**) isothermal treatment at 1420 °C; (**b**,**e**) isothermal treatment at 1400 °C; (**c**–**f**) isothermal treatment at 1390 °C.

Theoretical analysis of the effects of electromagnetic stirring on spherical grains stability is studied. The mechanism of grain refinement increases the critical radius for stability effected by electromagnetic stirring. On the basis of the stability theory of constitutional supercooling, the influence of EMF on the stability of equiaxed grains is investigated. The model of equiaxed grain in near liquidus melt under the influence of electromagnetic field is established.

The spherical coordinate system is shown in Figure 8. The center of the sphere is regarded as the origin of coordinates. Consider a globular initial nucleus with a radius R_0. The interface subject to time is given by:

$$r = R(\theta, \varphi, t) \tag{1}$$

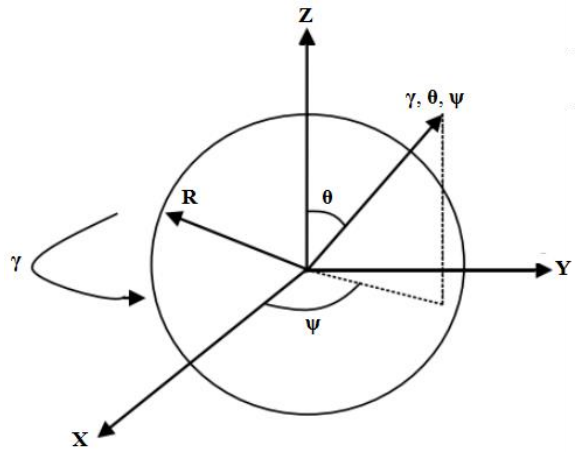

Figure 8. The spherical coordinate of undercooled melt.

The thermal and solute diffusion in the bulk liquid is under the influence of EMF. Equations (2)–(4) are the equations of the thermal and solute fields unaffected by interface morphological disturbance, this is the equation of the thermal and solute fields for pure diffusion. Based on the equation for pure

diffusion, the equation of the thermal and solute fields under the influence of EMF can be solved. When EMF is applied in the melt, there is a morphological disturbance at the solid–liquid interface. The thermal and solute field distribution of the disturbance are shown in the Equations (14)–(16).

$$U \cdot \nabla T_{\mathrm{L}} + S_{\mathrm{e}}^{\mathrm{L}}/k_{\mathrm{L}} = (k_{\mathrm{L}}/C_{\mathrm{pL}})\Delta T_{\mathrm{L}} \tag{2}$$

$$U_{\mathrm{S}} \cdot \nabla T_{\mathrm{S}} + S_{\mathrm{e}}^{\mathrm{S}}/k_{\mathrm{S}} = (k_{\mathrm{S}}/C_{\mathrm{pS}})\Delta T_{\mathrm{S}} \tag{3}$$

$$U \cdot \nabla C = D\Delta C \tag{4}$$

where U and U_{s} are the velocities in liquid and solid, respectively; T_{L} and T_{S} are the temperature profiles in liquid and solid, respectively; k_{L} and k_{S} are the thermal conductivities in liquid and solid, respectively; C_{pL} and C_{pS} are the specific heats in liquid and solid, respectively; C is the solute profile in liquid; $S_{\mathrm{e}} = E^2$. K_{e} is the heat per unit volume metal obtained per unit time; E is electromotive force and K_{e} is electrical conductivity. To solve the flow field around the initial nucleus, the velocities in r direction are 0, so the thermal and solute fields can be described as follows:

$$(\frac{\partial^2}{\partial r^2} + \frac{2}{r}\frac{\partial}{\partial r})T_L = \frac{S_{\mathrm{e}}^{\mathrm{L}} C_{\mathrm{pL}}}{k_{\mathrm{L}}^2} \tag{5}$$

$$(\frac{\partial^2}{\partial r^2} + \frac{2}{r}\frac{\partial}{\partial r})T_{\mathrm{S}} = \frac{S_{\mathrm{e}}^{\mathrm{S}} C_{\mathrm{pS}}}{k_{\mathrm{S}}^2} \tag{6}$$

$$(\frac{\partial^2}{\partial r^2} + \frac{2}{r}\frac{\partial}{\partial r})C = 0 \tag{7}$$

The boundary conditions at the interface follow:

$$T_{\mathrm{LI}} = T_{\mathrm{SI}} = T_{\mathrm{M}} + m_{\mathrm{L}} C_{\mathrm{I}} - \Gamma T_{\mathrm{M}} K \tag{8}$$

$$-h_\Delta \frac{\partial R}{\partial t} = k_{\mathrm{L}}(\frac{\partial T_{\mathrm{L}}}{\partial r})_{\mathrm{I}} - k_S(\frac{\partial T_{\mathrm{S}}}{\partial r})_{\mathrm{I}} \tag{9}$$

$$-C_{\mathrm{I}}(1-k_0)\frac{\partial R}{\partial t} = D(\frac{\partial C}{\partial r})_{\mathrm{I}} \tag{10}$$

where T_{LI}, T_{SI} and T_{M} are the temperature in liquid and solid at the interface and melt point, respectively; m_{L} the liquidus slope; C_{I} concentration at the interface; Γ Gibbs-Thomson coefficient; K curvature; δh_Δ latent heat; k_0 solute partition coefficient.

Then the heat diffusion and solute diffusion equations can be solved as follows.

$$\begin{aligned} T_{\mathrm{L}} = {} & \nu h_\Delta R_0^2/(k_{\mathrm{L}} r) - \tfrac{S_{\mathrm{e}}^{\mathrm{S}} C_{\mathrm{pS}} R_0^3}{3k_{\mathrm{L}} k_{\mathrm{S}} r} + \tfrac{S_{\mathrm{e}}^{\mathrm{L}} C_{\mathrm{pL}} r^2}{6k_{\mathrm{L}}^2} + T_{\mathrm{M}} + m_{\mathrm{L}} C_{\mathrm{I}} - \\ & 2\Gamma T_{\mathrm{M}}/R_0 - \nu h_\Delta R_0/k_{\mathrm{L}} + \tfrac{S_{\mathrm{e}}^{\mathrm{S}} C_{\mathrm{pS}} R_0^2}{3k_{\mathrm{L}} k_{\mathrm{S}}} - \tfrac{S_{\mathrm{e}}^{\mathrm{L}} C_{\mathrm{pL}} R_0^2}{6k_{\mathrm{L}}^2} \end{aligned} \tag{11}$$

$$\begin{aligned} T_{\mathrm{S}} = {} & \tfrac{S_{\mathrm{e}}^{\mathrm{S}} C_{\mathrm{pS}} r^2}{6k_{\mathrm{S}}^2} - \tfrac{S_{\mathrm{e}}^{\mathrm{L}} C_{\mathrm{pL}} R_0^3}{3k_{\mathrm{L}} k_{\mathrm{S}} r} + + T_{\mathrm{M}} + m_{\mathrm{L}} C_{\mathrm{I}} - \\ & 2\Gamma T_{\mathrm{M}}/R_0 + \tfrac{S_{\mathrm{e}}^{\mathrm{L}} C_{\mathrm{pL}} R_0^2}{3k_{\mathrm{L}} k_{\mathrm{S}}} - \tfrac{S_{\mathrm{e}}^{\mathrm{S}} C_{\mathrm{pS}} R_0^2}{6k_{\mathrm{S}}^2} \end{aligned} \tag{12}$$

$$C = vC_{\mathrm{I}} R_0 (1-k_0)(R_0/r - 1)/D + C_{\mathrm{I}} \tag{13}$$

Linear stability is analyzed through deciding whether the infinitesimal perturbation on the equiaxed grain interface grows or decays. The perturbation fields are written as follows:

$$T_{\mathrm{L}} = T_{\mathrm{L}}(Z) + \delta Y_{\mathrm{lm}} g_1(r) \tag{14}$$

$$T_{\mathrm{S}} = T_{\mathrm{S}}(Z) + \delta Y_{\mathrm{lm}} g_2(r) \tag{15}$$

$$C = C(Z) + \delta Y_{\mathrm{lm}} g_3(r) \tag{16}$$

where $T_{\mathrm{L}}(Z)$, $T_{\mathrm{S}}(Z)$ and $C(Z)$ are the steady-state solutions of thermal and solute diffusion equations for the interface, δ the amplitude of the perturbation, Y_{lm} a spherical harmonic. Substituting Equations (14)–(16) into Equations (2)–(4), respectively. $g_1(r)$, $g_2(r)$ and $g_3(r)$ can be solved. Substituting Equations (14)–(16) into Equations (8)–(10), respectively, the perturbation fields can be written as follows.

$$-h_\Delta \dot{\delta} Y_{\mathrm{lm}} = \delta Y_{\mathrm{lm}} (k_{\mathrm{L}} \frac{\partial g_1}{\partial r}|_{r=R_0} - k_S \frac{\partial g_2}{\partial r}|_{r=R_0}) + \frac{2vh_\Delta}{R_0} + \frac{k_{\mathrm{S}} S_{\mathrm{e}}^{\mathrm{L}} C_{\mathrm{pL}} - k_{\mathrm{L}} S_{\mathrm{e}}^{\mathrm{S}} C_{\mathrm{pS}}}{k_{\mathrm{L}} k_{\mathrm{S}}} \tag{17}$$

$$-C_I(1-k_0)\dot{\delta} Y_{\mathrm{lm}} = \delta Y_{\mathrm{lm}} D \frac{\partial g_3}{\partial r}|_{r=R_0} + \frac{2(1-k_0)vC_{\mathrm{I}}R_0^2}{(R_0-1)^3} \tag{18}$$

where v is velocity of the grain interface. Then, a combination of Equations (17) and (18) leads to the characteristic equation determining whether the perturbation grows or decays:

$$G = \frac{\dot{\delta}}{\delta} = \frac{G'}{(1-k_0)C_{\mathrm{I}}(k_{\mathrm{S}} S_{\mathrm{e}}^{\mathrm{L}} C_{\mathrm{pL}} - k_{\mathrm{L}} S_{\mathrm{e}}^{\mathrm{S}} C_{\mathrm{pS}})(R_0-1)^3 - 2(1-k_0)C_{\mathrm{I}} k_{\mathrm{L}} k_{\mathrm{S}} v h_\Delta [R_0^3 - (R_0-1)^3]} \tag{19}$$

The equiaxed grain interface subjected to infinitesimal perturbations holds stable if $G < 0$ is satisfied, and unstable if $G > 0$ satisfied. As $k_{\mathrm{S}} = \alpha_{\mathrm{S}} \rho C_{\mathrm{pS}}$, $k_{\mathrm{L}} = \alpha_{\mathrm{L}} \rho C_{\mathrm{pL}}$. Then $k_{\mathrm{S}} S_{\mathrm{e}}^{\mathrm{L}} C_{\mathrm{pL}} - k_{\mathrm{L}} S_{\mathrm{e}}^{\mathrm{S}} C_{\mathrm{pS}} = \rho C_{\mathrm{pL}} C_{\mathrm{pS}} E^2 (\alpha_{\mathrm{S}} K_{\mathrm{e}}^{\mathrm{L}} - \alpha_{\mathrm{L}} K_{\mathrm{e}}^{\mathrm{S}}) < 0$, the stability of equiaxed grain interface was determined by:

$$\begin{aligned} G' = \; & 2(1-k_0)C_{\mathrm{I}} k_{\mathrm{L}} k_{\mathrm{S}} v R_0^3 (k_{\mathrm{L}} \tfrac{\partial g_1}{\partial r}|_{r=R_0} - k_S \tfrac{\partial g_2}{\partial r}|_{r=R_0}) - \\ & \left[(k_{\mathrm{S}} S_{\mathrm{e}}^{\mathrm{L}} C_{\mathrm{pL}} - k_{\mathrm{L}} S_{\mathrm{e}}^{\mathrm{S}} C_{\mathrm{pS}} + 2k_{\mathrm{L}} k_{\mathrm{S}} v h_\Delta)(R_0-1)^3 \right] D \tfrac{\partial g_3}{\partial r}|_{r=R_0} \end{aligned} \tag{20}$$

The equiaxed grain interface subjected to infinitesimal perturbations holds stable if $G' > 0$ is satisfied, and unstable if $G' < 0$ satisfied. Under the influence of EMF, the forced convection in the melt could decrease the normal gratitude of the perturbations on the temperature and concentration field, which makes $G' > 0$ established. From these theoretical analysis, one can conclude that the stirring and heating caused by the EMF change the crystal nucleation and growth condition, promote the formation of globular microstructure and suppress the occurrence of dendritic microstructure.

3.4. Effects of the Structure Transition on the Microstructures

In order to study the grain refinement mechanism near liquidus temperature, the structure factors $S(Q)$ of liquid Ni-Cr-W superalloy at different temperatures have been measured by a high-temperature X-ray diffractometer. The results are shown in Figure 9.

As the temperature decreases from 1420 °C to 1390 °C, the intensity of the main peak gradually increases, and the disordering degree falls. There is no pre-peak on the structure factor curve at 1420 °C, 1410 °C and 1390 °C, as shown in Figure 9, and a clear pre-peak before the main peak exists on the curve of structure factor and original intensity of Ni-Cr-W superalloy at the temperature of 1480 °C and 1400 °C. It is universally considered that these pre-peaks are associated with MRO structure and intermetallic compound [28]. This MRO structure exhibits strong temperature dependence. To deeply illustrate the temperature dependencies of the MRO structure, $S_{\text{pre-peak}}/S_{\text{total}}$, the ratio of the pre-peak area (the integrated height of the original $S(Q)$ curve, with $Y = 0$ as the baseline) to the total area of the $S(Q)$ curve is adopted. The ratio of the pre-peak area at 1400 °C is considerably larger than that at 1480 °C, which indicates that the number of MRO clusters at 1400 °C is greater than that at 1480 °C. Meanwhile, two kinds of MRO clusters at 1400 °C and 1480 °C are different. MRO clusters at 1400 °C must be caused by the liquid/solid transition of the solidification process and intermetallic compound. Ni_2Cr and Ni_3Cr_2 chemical compounds are formed near the liquidus in the Ni-Cr system,

and such clusters can be regarded as "nuclei" of the matrix phase. This leads to the formation of fine grain microstructure, as shown in Figure 1d. First-order structural phase transition at 1480 °C may be due to carbides, because the Ni-Cr-W superalloy is a carbide strengthened alloy.

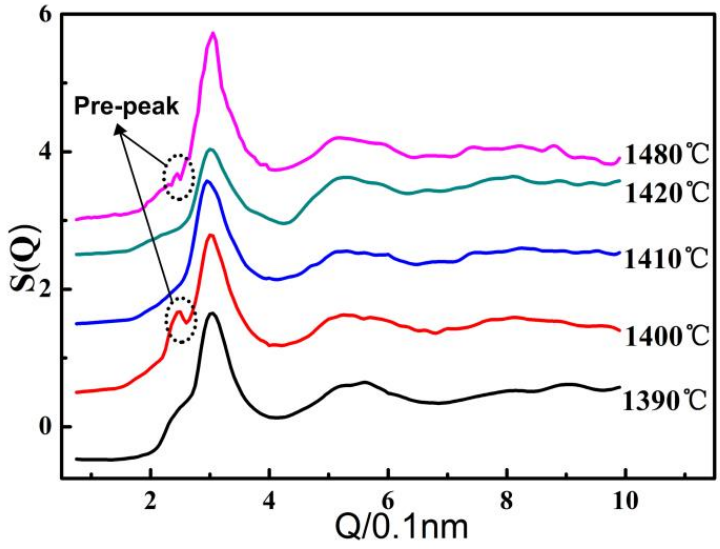

Figure 9. Temperature dependence of total structure factors of the Ni-Cr-W superalloy.

Above all, although the cooling rate influences the solidification structure, the most important factor which affects the microstructure is the treatment temperature near liquidus before solidification, which leads to the non-dendrite equiaxed microstructure. The mechanisms of the grain refinement can be summarized as follows. During the melt holding at an appropriate time in the transition state region, the melt temperature field becomes more uniform, which also makes small phase fluctuation. This means that the quantities of clusters increase in the melt and its distribution are more uniform. The formation of equiaxed and non-dendritic grains in ingots or castings near liquidus is believed as the effect of clusters on nucleation. Under a certain degree of undercooling, the size of the clusters reaches the critical nucleation radius. Summarizing, equiaxed grains in castings can originate from both high nucleation derived from atom cluster and uniform solute field.

4. Conclusions

In summary, the resulting microstructure is composed of globular, equiaxed grains distributed in the solidification structure, the average grain size is 60 μm, and the value of CSF is 0.95 when the melt is subjected to heat treatment of 10 min at 1400 °C. In contrast, casting of the alloy around its liquidus temperature could result in the usual dendritic structure. And the sizes and shapes of the grains around the liquidus temperature are not homogeneous. Due to the uniform temperature, solute field and the high density of the secondary nuclei prior to solidification under electromagnetic field, grain refinement can be effectively achieved. Finally, the emergence of clusters contributes to increase nucleation rate and the grain refinement.

Author Contributions: Z.G. carried out the experimental, analysis and writing works, W.G., C.Z. and W.Z. are responsible for formal analysis work, while J.T. provides guidance on the experimental works and the write-up.

Funding: This research was funded by National Natural Science Foundation of China (51804251), China Postdoctoral Science Foundation (No. 2017M613165), Research Project of state key laboratory of solidification processing (No. SKLSP201727), Science Foundation for the Excellent Youth scholars (No. 2018YQ3-05) and The National Key Research and Development Program of Shanxi Province (No. 2018GY-163).

Acknowledgments: The authors appreciate Yuan Yu at the Institute of chemical physics, Chinese Academy of Sciences, for discussing the microstructural evolution of this alloy.

Conflicts of Interest: The authors declare no conflict of interest.

References

1. Ma, Y.; Sun, J.H.; Xie, X.S.; Hu, Y.H.; Zhao, J.C.; Yan, Y.J. An investigation on fine-grain formation and structural character in cast IN718 superalloy. *J. Mater. Process. Technol.* **2003**, *35*, 137–141. [CrossRef]
2. Jamili, A.M.; Zarei-Hanzaki, A.; bedi, A.; Minárik, P.; Soltani, R. The microstructure texture and room temperature mechanical properties of friction stir processed Mg-Y-Nd alloy. *Mater. Sci. Eng. A* **2017**, *690*, 244–253. [CrossRef]
3. Liu, X.Q.; Zhao, D.S.; Ye, L.; Zhuang, Y.L.; Gao, S.B. Effect of Er contents on the microstructure of long period stacking ordered phase and the corresponding mechanical properties in Mg-Dy-Er-Zn alloys. *Mater. Sci. Eng. A* **2018**, *718*, 461–467. [CrossRef]
4. Li, M.; Tamura, T.; Omura, N.; Murakami, Y.; Tada, S. Grain refinement of AZCa912 alloys solidified by an optimized electromagnetic stirring technique. *J. Mater. Process. Technol.* **2016**, *235*, 114–120. [CrossRef]
5. Haghayeghi, R.; Nastac, L. On microstructural refinement of an AA7449 aluminium alloy through shearing above liquidus temperature. *Mater. Lett.* **2011**, *65*, 3230–3233. [CrossRef]
6. Xu, J.; Dang, B.; Fan, D.; Jian, Z. Effect of Melt superheating treatment on the latent heat release of Sn. *Metal. Mater. Trans. A* **2017**, *43*, 1133–1138. [CrossRef]
7. Hu, X.G.; Zhu, Q.; Atkinson, H.V.; Lu, H.X.; Zhang, F. A time-dependent power law viscosity model and its application in modelling semi-solid die casting of 319s alloy. *Acta Mater.* **2017**, *124*, 410–420. [CrossRef]
8. Srirangam, P.; Kramer, M.J.; Shankar, S. Effect of strontium on liquid structure of Al-Si hypoeutectic alloys using high-energy X-ray diffraction. *Acta Mater.* **2011**, *59*, 503–513. [CrossRef]
9. Wannasin, J.; Canyook, R.; Wisutmethangoon, S.; Flemings, M.C. Grain refinement behavior of an aluminum alloy by inoculation and dynamic nucleation. *Acta Mater.* **2013**, *61*, 3897–3903. [CrossRef]
10. Xu, Q.Y.; Yang, C.; Zhang, H.; Yan, X.W.; Tang, N.; Liu, B.C. Multiscale modeling and simulation of directional solidification process of Ni-Based superalloy turbine blade casting. *Metals* **2018**, *8*, 632. [CrossRef]
11. Xia, K.; Tausig, G. Liquidus casting of a wrought aluminum alloy 2618 for thixoforming. *Mater. Sci. Eng. A* **1998**, *246*, 1–10. [CrossRef]
12. Belyakov, A.; Tikhonova, M.; Dolzhenko, P.; Sakai, T.; Kaibyshev, R. On kinetics of grain refinement and strengthening by dynamic recrystallization. *Adv. Eng. Mater.* **2018**, *27*, 12–16. [CrossRef]
13. Maxwell, I.; AHellawell, A. Simple model for grain refinement during solidification. *Acta Mater.* **1975**, *8*, 229–237. [CrossRef]
14. Zuo, Y.B.; Cui, J.Z.; Zhao, Z.H.; Zhang, H.T.; Li, L.; Zhu, Q.F. Mechanism of grain refinement of an Al-Zn-Mg-Cu alloy prepared by low-frequency electromagnetic casting. *J. Mater. Sci.* **2012**, *47*, 5501–5508. [CrossRef]
15. Ali, Y.; Qiu, D.; Jiang, B.; Pan, F.; Zhang, M.X. Current research progress in grain refinement of cast magnesium alloys: A review article. *J. Alloys Compd.* **2015**, *619*, 639–651. [CrossRef]
16. Du, L.F.; Zhang, P.; Yang, S.M.; Gao, Z.T.; Chen, J.; Du, H.L. Phase-field simulation on dendritic to semi-circular morphology transition induced by forced liquid flow. *Appl. Phys. A* **2018**, *124*, 211–217. [CrossRef]
17. Gao, Z.T.; Hu, R.; Wang, J.; Li, J.S. Heredity of medium-range order structure from melts to the microstructure of Ni-Cr-W superalloy. *Appl. Phys. A* **2015**, *120*, 183–189. [CrossRef]
18. Wu, Y.Q.; Bian, X.F.; Meng, Q.G.; Zhao, Y. A critical transition state in liquid metals. *Mater. Lett.* **2007**, *112*, 2434–2438. [CrossRef]
19. Bai, Y.W.; Bian, X.F.; Lv, X.Q.; Pan, S.P.; Qin, J.Y.; Qin, X.B.; Hu, L.N. Heredity of medium-range order structure from melts to amorphous solids. *J. Appl. Phys.* **2012**, *112*, 083524. [CrossRef]
20. Couillard, M.; Pratontep, S.; Palmer, R.E. Metastable ordered arrays of size-selected Ag clusters on graphite. *Appl. Phys. Lett.* **2003**, *82*, 2595–2599. [CrossRef]
21. Liu, Q.; Zhao, X.; Zhang, X.; Wang, H. Effect of thermal aging on mechanical properties of a bainitic forging steel for reactor pressure vessel. *Mater. Sci. Eng. A* **2018**, *720*, 176–180. [CrossRef]
22. Smith, T.M.; Bonacuse, P.; Sosa, J.; Kulis, M.; Evans, L. A quantifiable and automated volume fraction characterization technique for secondary and tertiary γ' precipitates in Ni-based superalloys. *Mater. Charact.* **2018**, *140*, 86–94. [CrossRef]
23. Liu, X.J.; Pan, Y.W.; Chen, Y.C.; Han, J.J.; Yang, S.Y. Effects of Nb and W additions on the microstructures and mechanical properties of novel γ/γ' Co-V-Ti-Based superalloys. *Metals* **2018**, *8*, 563. [CrossRef]

24. Wang, Y.; Zhao, S.; Zhao, X.; Zhao, Y. Effect of hot deformation on γ″ and δ phase precipitation of Inconel 718 alloy during deformation&isothermal treatment. *J. Alloys Compd.* **2017**, *716*, 191–200.
25. Haghayeghia, R.; Zoquib, E.J.; Greenc, N.R.; Bahaia, H. An investigation on DC casting of a wrought aluminium alloy at below liquidus temperature by using melt conditioner. *J. Alloys Compd.* **2010**, *502*, 382–386. [CrossRef]
26. Li, M.J.; Tamura, T.; Omura, N.K.; Miwa, K.J. An investigation on DC casting of a wrought aluminium alloy at below liquidus temperature by using melt conditioner. *J. Alloys Compd.* **2009**, *487*, 382–386.
27. Li, T.; Huang, W.D.; Lin, X. Microstructure and phase evolution in laser rapid forming of a functionally graded Ti-Rene88DT alloy. *Acta Mater.* **2006**, *54*, 1901–1915.
28. Roik, O.S.; Samsonnikov, O.V.; Kazimirov, V.P.; Sokolskii, V.E. Medium-range order in Al-based liquid binary alloys. *J. Mol. Liq.* **2010**, *151*, 42–49. [CrossRef]